ADVANCED OPTICAL MATERIALS
www.advopticalmat.de

High Refractive Index Chalcogenide Hybrid Inorganic/Organic Polymers for Integrated Photonics

Abhinav Nishant, Kyung-Jo Kim, Sasaan A. Showghi, Roland Himmelhuber, Tristan S. Kleine, Taeheon Lee, Jeffrey Pyun, and Robert A. Norwood**

Optical polymer-based integrated photonic devices are gaining interest for applications in optical packaging, biosensing, and augmented/virtual reality (AR/VR). The low refractive index of conventional organic polymers has been a barrier to realizing dense, low footprint photonic devices. The fabrication and characterization of integrated photonic devices using a new class of high refractive index polymers, chalcogenide hybrid inorganic/organic polymers (CHIPs), which possess high refractive indices and lower optical losses compared to traditional hydrocarbon-based polymers, are reported. These optical polymers are derived from elemental sulfur via the inverse vulcanization process, which allows for inexpensive monomers to be used for these materials. A facile fabrication strategy using CHIPs via lithography is described for single-mode optical waveguides, Y junction splitters, multimode interferometers (MMIs), and high Q factor ring resonators, along with device characterization. Furthermore, propagation losses of 0.4 dB cm^{-1} near 1550 nm wavelength, which is the lowest measured loss in non-fluorinated optical polymer waveguides, coupled with the benefits of low cost materials and manufacturing are reported. Ring resonators with Q factor on the order of 6×10^4 and cavity finesse of 45, which are some of the highest values reported for optical polymer-based ring resonators, are also reported.

1. Introduction

Optical polymers have long been used in integrated photonics,[1,2] as this class of materials offers wide tunability of both optical and thermomechanical properties via compositional variations, while retaining low absorption loss at telecom wavelengths.[3–8] Furthermore, polymeric materials are relatively inexpensive to synthesize and are amenable to a wider range of fabrication techniques for device fabrication in contrast to inorganic counterpart materials, such as silicon (Si) and silicon nitride (SiN). As a result, optical polymers are increasingly seen as cost-effective solutions for manufacturing photonic devices in high volume. Despite these numerous processing advantages, optical polymer materials for integrated photonics remain limited relative to inorganic materials with respect to critical optical properties, especially refractive index (n, or RI). The vast majority of current optical polymers have a refractive index ranging between 1.3–1.6 at telecom wavelengths, which is significantly lower than the RI values of SiN, lithium niobate ($n \approx 2.0$–2.2), or higher RI materials such as Si,[9,10] indium phosphide, or germanium ($n \approx 3.5$–4.0). Because of these dramatically lower RI values, on-chip integrated photonic components, such as waveguides or ring resonators fabricated using optical polymers require much larger feature sizes beyond what is tenable for numerous on-chip device systems and preclude the fabrication of curved features with tight bend radii which are essential integrated optical elements. With an ever-increasing demand for high density integrated optical circuitry, the large areal footprint of state-of-the-art polymer devices due to limited RI contrast remains a critical limitation toward realizing all-polymer photonic circuits for high density interconnects and integration. Hence, there is a compelling technological need for high RI polymers ($n >> 1.6$ at telecom at 1310 and 1550 nm) that are amenable to thin film processing and high throughput nano/microfabrication techniques (e.g., photolithography). There are a handful of inorganic materials, such as Hydex glass[11,12] and silicon oxynitride (SiON),[13] which have been studied to create inexpensive, earth-abundant inorganic materials that achieve RI values ranging from $n = 1.6$–2.0 at telecom wavelengths. Furthermore, recent work on solution-processable chalcogenide glasses (ChGs) has been explored to create thin films and integrated photonic components, such as single-mode waveguides in the mid-wave infrared (MWIR), which exploit the high RI and high transparency ChGs.[14–17] However, fabrication processes for these materials remain non-trivial, requiring multi-step high temperature methods, or the use of unconventional toxic solvents which has limited wide-scale deployment. Numerous

A. Nishant, K.-J. Kim, S. A. Showghi, R. Himmelhuber, R. A. Norwood
J. C. Wyant College of Optical Sciences
University of Arizona
Tucson, AZ 85721, USA
E-mail: rnorwood@optics.arizona.edu
T. S. Kleine, T. Lee, J. Pyun
Department of Chemistry and Biochemistry
University of Arizona
Tucson, AZ 85721, USA
E-mail: jpyun@email.arizona.edu
The ORCID identification number(s) for the author(s) of this article can be found under https://doi.org/10.1002/adom.202200176.

DOI: 10.1002/adom.202200176

efforts have been made to prepare optical polymers with high RI for use in consumer optics ($n \approx 1.6$–1.7) or holography[18–25] however the development of high RI polymers for integrated photonics remains an important technological target. Optical ring resonators have been fabricated from commercially available photopolymers, such as SU8 ($n = 1.57$), however, polymer-based ring resonators with both reduced dimensions and high Q-factor resonances have not been achieved.[26–28]

An attractive candidate for integrated photonics are solution-processable materials based on chalcogenide hybrid inorganic/organic polymers (CHIPs), which are a recently developed class of polymers possessing high RI values (n = 1.7–2.1) and improved optical transparency across the visible-near infrared-shortwave infrared wavelength range.[29–31] These materials are the first of their kind chalcogenide-based polymers, which share many of the attractive properties of chalcogenide glasses[14,15,32] while also being amenable to solution processing and classical lithographic techniques for fabrication of integrated photonic devices. CHIPs are prepared by the direct copolymerization of elemental sulfur and selenium with organic olefinic comonomers via a process termed, inverse vulcanization.[29,30] The unusually high content of S–S bonds in the polymeric backbone impart both high RI values and unprecedented optical transparency in the infrared spectrum due to the reduced organic content in the material and the shifted absorbances of S–S bonds into the IR spectral window. Thus far, the primary interest in CHIPs has exploited the enhanced mid-wave and long-wave IR transparency for thermal imaging studies of molded bulk optical windows, which were the first examples of using synthetic polymers for this application.[31,33] Melt-processing to fabricate poly(sulfur-*random*-1,3-diisopropenylbenzene) (poly(S-*r*-DIB)) polarizers for use in the IR have also been demonstrated.[36] Both the high RI and solution processability of CHIPs based on 1,3-diisopropylbenzene (DIB) comonomers with sulfur and selenium were exploited to prepare highly reflective one-dimensional photonic crystals in the SWIR from 1000–2000 nm.[34,35,37] However, to the best of our knowledge, there have not been reports on the fabrication of CHIPs photonic components and devices for single-mode photonic applications, which is essential for integrated photonics. Single-mode waveguides fabricated using high refractive index polymers can have a multitude of applications, including low-loss photonic interconnects,[7,8] compact thermo-optic devices,[38] multiplexers/demultiplexers, optical phased arrays,[39] biosensors,[40] etc. The use of high content sulfur polymers with reduced C–H content also offers a new and inexpensive route to low-loss optical polymeric devices that have classically required the use of fluorinated polymers.[1,2]

Herein, we demonstrate a facile nanofabrication process for the creation of photonic devices from CHIPs. The solution processability of our first-generation CHIPs materials based on poly(sulfur-*random*-1,3-diisopropenylbenzene) (poly(S-*r*-DIB) was exploited to prepare thin films on silicon substrates to fabricate low-loss, single-mode polymer waveguides, optical splitters, and ring resonators for the first time via lithography and dry etching. The high RI of these optical polymers was particularly advantageous to reduce the feature size of ring resonators to radii on the order of 100 µm with high Q-factors exceeding 5×10^4, illustrating the utility of these new

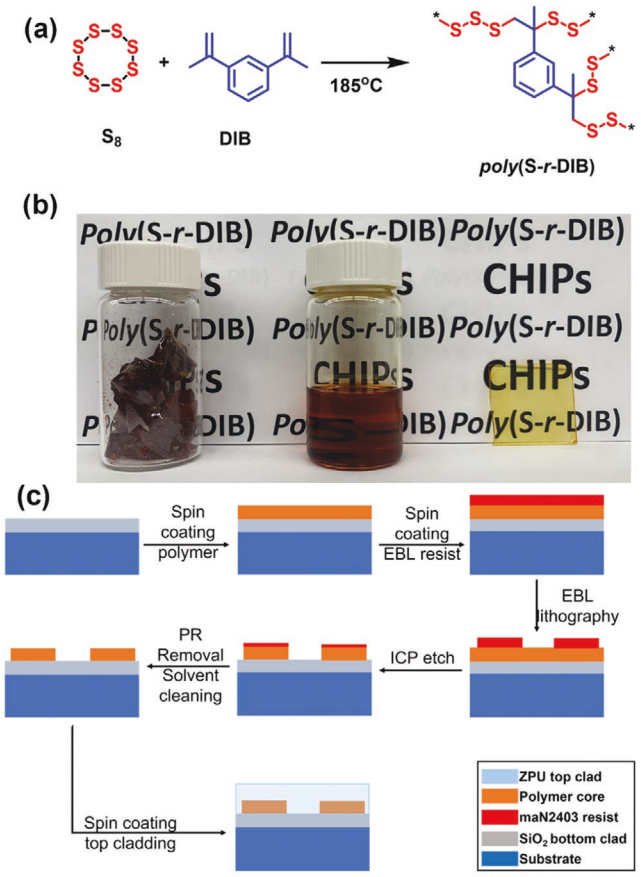

Figure 1. a) Synthetic scheme for inverse vulcanization of 1,3-diisopropenylbenzene to form *poly*(S-*r*-DIB); b) digital images of poly(S-*r*-DIB) (left), poly(S-*r*-DIB) solution in chlorobenzene (center, c = 10 mg mL^{-1}) and poly(S-*r*-DIB) thin film (2 µm) on a glass substrate; and c) schematic process for CHIPs device fabrication via spin coating and e-beam lithographic methods which utilized a high RI core of poly(S-*r*-DIB) layer (d = 450 nm) and a top cladding layer of ZPU ($d \approx 4$ µm).

organic/inorganic hybrid materials for integrated photonics. To our knowledge, this is one of the few reports on using a high RI optical polymer for integrated photonics and the first report on the use of CHIPs for the fabrication of photonic devices.

2. Results and Discussion

2.1. Fabrication of Passive Photonic Devices Made Using CHIPs

The high RI material used for the core layer in photonic device components was a poly(S-*r*-DIB) copolymer with a composition of 70-wt% sulfur as prepared by the inverse vulcanization process,[29] which was chosen due to its comparatively higher RI (n = 1.75 at 1550 nm) and lower optical losses at 1310 and 1550 nm relative to conventional optical plastics as we previously reported[31] (**Figure 1**a). The inverse vulcanization process is essentially a bulk-free radical polymerization using molten sulfur as both the reaction medium and comonomer with organic olefinic compounds. In contrast to other solution-processable ChGs (e.g., As_2S_3),[14] or other high RI inorganic

materials, thin films of poly(S-*r*-DIB) could be prepared by spin-coating of concentrated polymers solution made from conventional organic solvents (e.g., chlorobenzene, $c = 350$ mg mL^{-1}), which enabled controllable deposition of high RI core layers (film thickness $d = 0.2$–2.0 µm) at varying rotating substrate speeds during spin coating (see Figure 1b for example of spin-coated film on glass).

The first step in the fabrication process was a computational simulation of various device dimensions which was conducted using eigenmode solver software packages (Fimmwave, Photon Design, and Lumerical MODE solutions). From these simulated specifications, the fabrication of single-mode waveguides, 1 × 2 MMI couplers, Y branches, and ring resonators were then conducted using a combination of spin coating, electron-beam lithography (EBL), and reactive-ion etching as detailed in the experimental section (see the Experimental Section below). To achieve appreciable refractive index contrast in these devices ($\Delta n \approx 0.4$), cladding layers of SiO_2 ($n = 1.44$ at 1550 nm) and ZPU ($n = 1.43$ at 1550 nm) were used. The ZPU top cladding was deposited on top of the core layer via spin coating (d ≈ 4 µm) followed by UV curing under N_2 atmosphere. Lithographic structuring of the core layer was achieved by spin coating of poly(S-*r*-DIB) onto SiO_2 bottom clad films on a carrier silicon substrate, followed by solution deposition, EBL of the photoresist layer (maN2403), and reactive ion etching to create the desired device architecture (Figure 1c). SEM of poly(S-*r*-DIB) waveguides on SiO_2 confirmed that the desired feature sizes of the high RI core layer were obtained (height = 450 nm, width = 2 µm, **Figure 2**a). The image does not include the ZPU top cladding layer. Similar overall dimensions were designed and imaged by SEM of the 1 × 2 MMI device confirming the successful fabrication of the input bus and output waveguide elements (Figure 2b). Y-splitting components were also successfully prepared as confirmed, where SEM imaging clearly discerned the critical junction of the output bend sections (Figure 2c). Finally, the preparation of poly(S-*r*-DIB) ring resonator structures was observed to be successful from SEM imaging confirming the geometry and target radius (200 µm) were fabricated, along with the coupling of the resonator to the bus waveguide (Figure 2d).

2.2. Characterization of High RI Polymer Waveguides

Optical waveguides are the fundamental building blocks of any photonic integrated circuit (PIC). Every photonic platform requires the use of low-loss, single-mode optical waveguides. The performance of the waveguides is determined by the propagation loss which is dependent on the optical absorption loss of the material, and optical scattering loss due to sidewall roughness. Since the material absorption is inherent to the material, the propagation loss is generally limited by the scattering loss. Hence, for waveguides with low propagation loss, sidewall roughness has to be minimized by optimizing the fabrication process. To test the robustness of our fabrication process, we have fabricated single-mode ridge waveguides

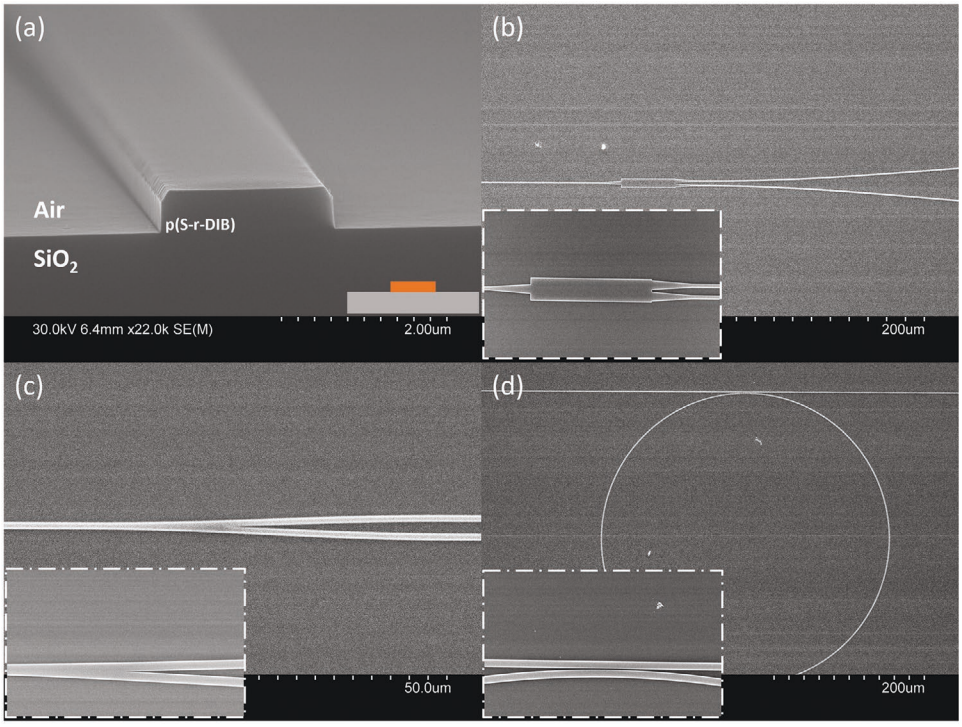

Figure 2. SEM images of the fabricated devices. a) Cross-section of the waveguide showing straight sidewalls and low etch roughness of the poly(S-r-DIB) core layer without the ZPU cladding layer. Inset cartoon represents patterned high RI core layer on glass. b) 1 × 2 MMI device with the input bus waveguide and output S-bends; inset shows the MMI structure. c) Y splitter with the input bus waveguide and output waveguides; inset shows the splitter junction with excellent lithography. d) Ring resonator with 200 µm radius; inset shows the coupling region between the bus waveguide and the top section of the ring.

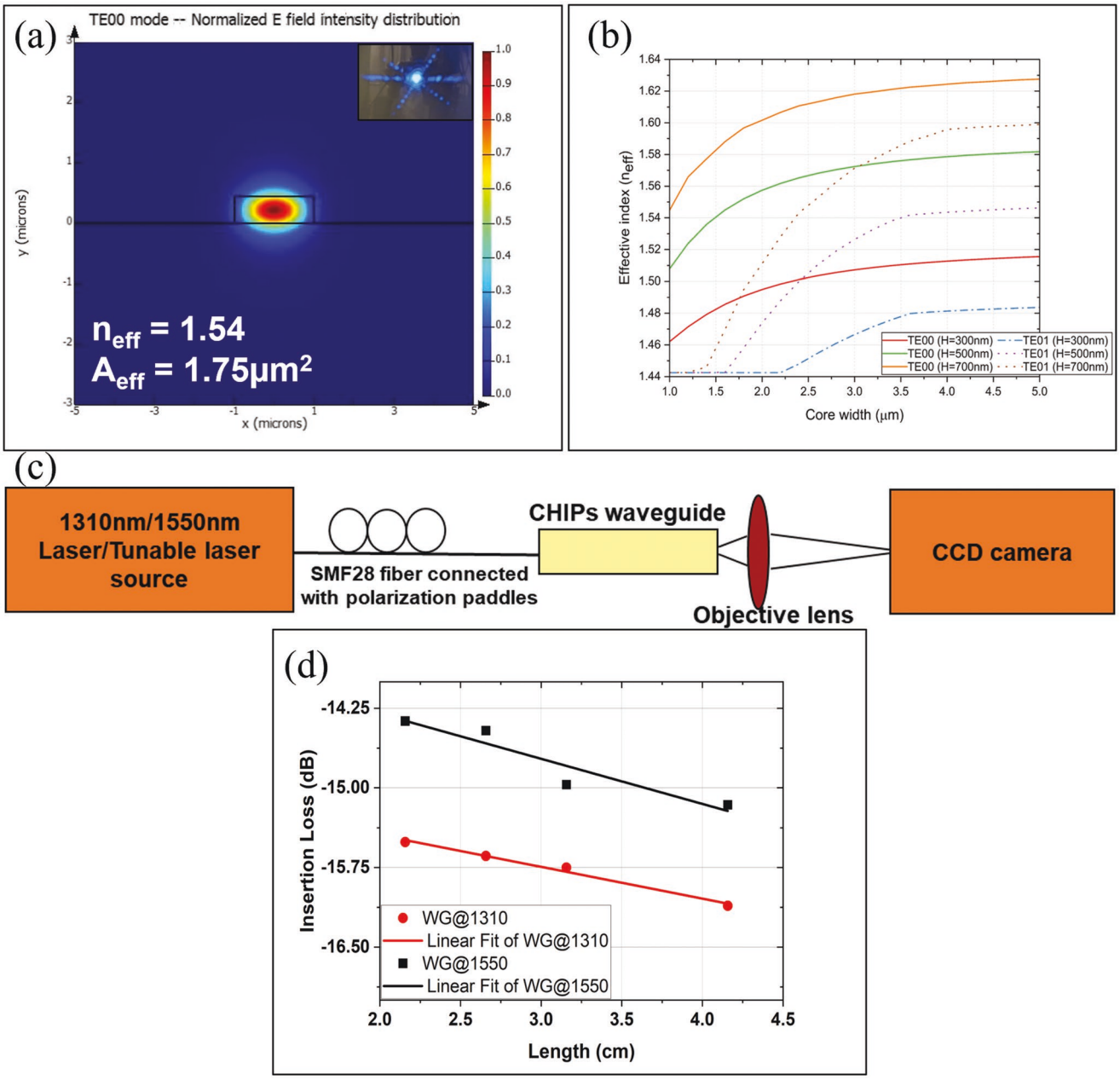

Figure 3. a) Simulated electric field distribution for fundamental TE mode of the waveguide; inset shows the output mode imaged by an InGaAs camera; b) simulated effective index as a relation of core width for three different film thicknesses; c) experimental setup for imaging the CHIPs waveguide mode profile. For measuring the power, the output side was replaced with SMF28 fiber and a power meter; and d) characterization of propagation loss in the waveguide by the cutback method at 1310 and 1550 nm wavelength.

using poly(S-*r*-DIB) as the core material. The waveguides were designed using a Fimmwave finite-difference mode (FDM) solver where these simulations predicted that waveguides with cross-sectional dimensions of 2 μm width and 0.45 μm height would afford single-mode guiding. The chosen thickness of the waveguides is easily achievable by one-step spin coating of a high quality thin film with an upper limit of around 2–3 μm. Similarly, the waveguide width is large enough to be easily resolved by any standard lithography tool. The effective index of this waveguide was calculated to be n_{eff} = 1.54, along with a group index of n_g = 1.73 at 1550 nm. Due to the high RI of the polymer core, the devices have high confinement of light resulting in low footprint devices; the simulated mode intensity profile is shown below in **Figure 3**a, with the inset showing the optically imaged mode of the fabricated waveguide clearly demonstrating single-mode operation. The effective index of the fundamental and the first-order TE modes was calculated as a function of waveguide core width for different film thicknesses (h = 300, 500, and 700 nm) to understand the single-mode guiding condition for the waveguide geometry (Figure 3b). A

series of serpentine waveguides with lengths varying from 20 to 40 mm were made on the same sample to measure the propagation loss via classical cutback methods. The power was measured for waveguides of varying lengths, whereas reference, input, and output fibers were coupled together with index-matching oil to determine the reference power. The total insertion loss was calculated by subtracting the reference power from the output power for each waveguide. The final insertion loss when plotted against the length of each device, giving us a linear curve with excellent goodness of fit, R^2 value > 0.95, and estimated propagation loss of 0.3 dB cm^{-1} at 1310 nm and 0.42 dB cm^{-1} at 1550 nm wavelength, as shown in Figure 3d. These optical losses were considerably less than classical hydrocarbon polymer-based waveguides that generally exhibit a lower loss limit of ≈ 1 dB cm^{-1} at 1550 nm due to the presence of vibrational overtones from C–H bonds at telecom wavelengths. The observed reduction of the propagation loss in poly(S-*r*-DIB) below 1 dB cm^{-1} can be directly attributed to the high content of the S–S bond in these organic/inorganic hybrid polymers and the reduced content of organic comonomer units. The coupling loss is about 7–8 dB coupling per facet which could be further reduced in principle by using UHNA fibers and/or patterning edge couplers on the chip. A schematic of the optical characterization setup used is shown in Figure 3c. The measurement confirms the low absorption loss of the material and reduced scattering loss due to the low sidewall roughness obtained by using an optimized etching recipe. These collective findings point to the advantages of using high RI CHIPs as a new class of polymers for waveguide fabrication which to our knowledge is the first report of this type of demonstration with integrated photonics.

2.3. 1 × 2 Splitters from CHIPs

Another important element of PICs are splitters which divide the guided light into equal intensity between two arms. Two of the most common splitters are multimode interference (MMI) splitters and Y junction splitters. The key requirement of the splitters is to have minimal additional insertion loss and equal splitting between the two arms of the device. The splitters were designed using Fimmwave eigenmode expansion (EME) software, FIMMPROP. For the 1 × 2 MMI, the optimized length and width of the MMI section were found to be 60 and 10 µm, respectively. 20 µm long linear taper sections were added at the input and output port with the width linearly varying from 2 to 4 µm, which minimizes the insertion loss further. The center-to-center separation of the output ports is 5 µm, and the optimized simulated structure has a low excess insertion loss of 0.08 dB at 1550 nm with 50% power splitting between the two output ports. The 2D electric field distribution of the MMI coupler is shown in **Figure 4**a. Y junction splitters were also designed using FIMMPROP. The optimized structure has two S bends with 200 µm bend radii splitting from a single-mode waveguide which separates into two single-mode waveguides with a 5 µm separation between them. The simulated excess insertion loss of the Y branch is 0.1 dB at 1550 nm, and the 2D electric field distribution is shown in Figure 4c. To measure the transmission in each output port of the MMI and Y splitters, S bends with 1 mm length and 100 µm separation followed by straight waveguides were added to the design so that the output fiber can access the two arms. The large radii of the S bends result in negligible loss and does not affect the device performance. The MMI and Y splitters were characterized by measuring the output power in each arm of the splitters across multiple devices and the loss is averaged. To calculate the additional insertion loss due to the structures, the output power of a reference straight waveguide is measured and subtracted from the output power from the two arms of the splitters. Since the splitters are expected to have equal splitting, the ideal insertion loss in each arm should be 3 dB. The final excess loss measured for the MMI per output port is 0.1 dB. Using similar steps, the average loss measured in each arm of the Y junction splitter is 0.2 dB per port. The results were repeated across three different devices, and the measurement error is estimated to be roughly 0.06 dB for MMI and 0.04 dB for Y splitter. The devices have excellent broadband performance with the simulated broadband response of over 1 µm wavelength range, owing to the low dispersion of the core p(S-*r*-DIB) material and high confinement of light in the waveguides. Figure 4b,d below shows the measured power of the splitters across the C-band wavelength range.

2.4. Characterization of High RI Polymeric Ring Resonators

Ring resonators are useful photonic devices with wide-ranging applications including optical delay lines, biosensing, and high quality cavities for active devices. Furthermore, the performance of these photonic components, most commonly used as integrated photonic filters, is highly sensitive to the nanofabrication methods used to fabricate the devices, making them well-suited for the evaluation of new optical materials. In addition, the dimensions of the ring resonator are critically associated with the RI of the active core material, where higher RI materials enable a reduction of the ring radius. As discussed earlier, ring resonators fabricated from classical lower RI polymers ($n < 1.6$) required ring resonator radii exceeding 1 mm,[28] while the use of ChG's,[14] or high RI CHIPs from poly(S-*r*-DIB) ($n = 1.75$) enable dramatic reduction of the ring resonator radii to below 0.1 mm. For all pass ring resonators (the most common type), the input light from an external laser is launched into the input bus waveguide which guides the light across the length of the chip. A ring of fixed radius is fabricated proximal to the bus waveguide (the typical gap between bus and ring > 1 µ). The input light guided in the bus waveguide can be evanescently coupled into the ring resonator by careful design of the cavity and modulation of the coupling conditions. Depending on the gap dimensions, shape, and dimensions of the ring cavity and the input bus waveguide; the resonance wavelength and the free spectral range (FSR) of the cavity are carefully selected. Narrow linewidth of the resonance peak, that is, the full width half maximum (FWHM), is highly desired. The ratio of the resonance wavelength and FWHM gives us the Q factor of the ring, which is a critical parameter to assess the quality of the fabrication as well as the effectiveness of the coupling schemes employed in the device design. Another important parameter is finesse which is the ratio of FSR and FWHM. While there are

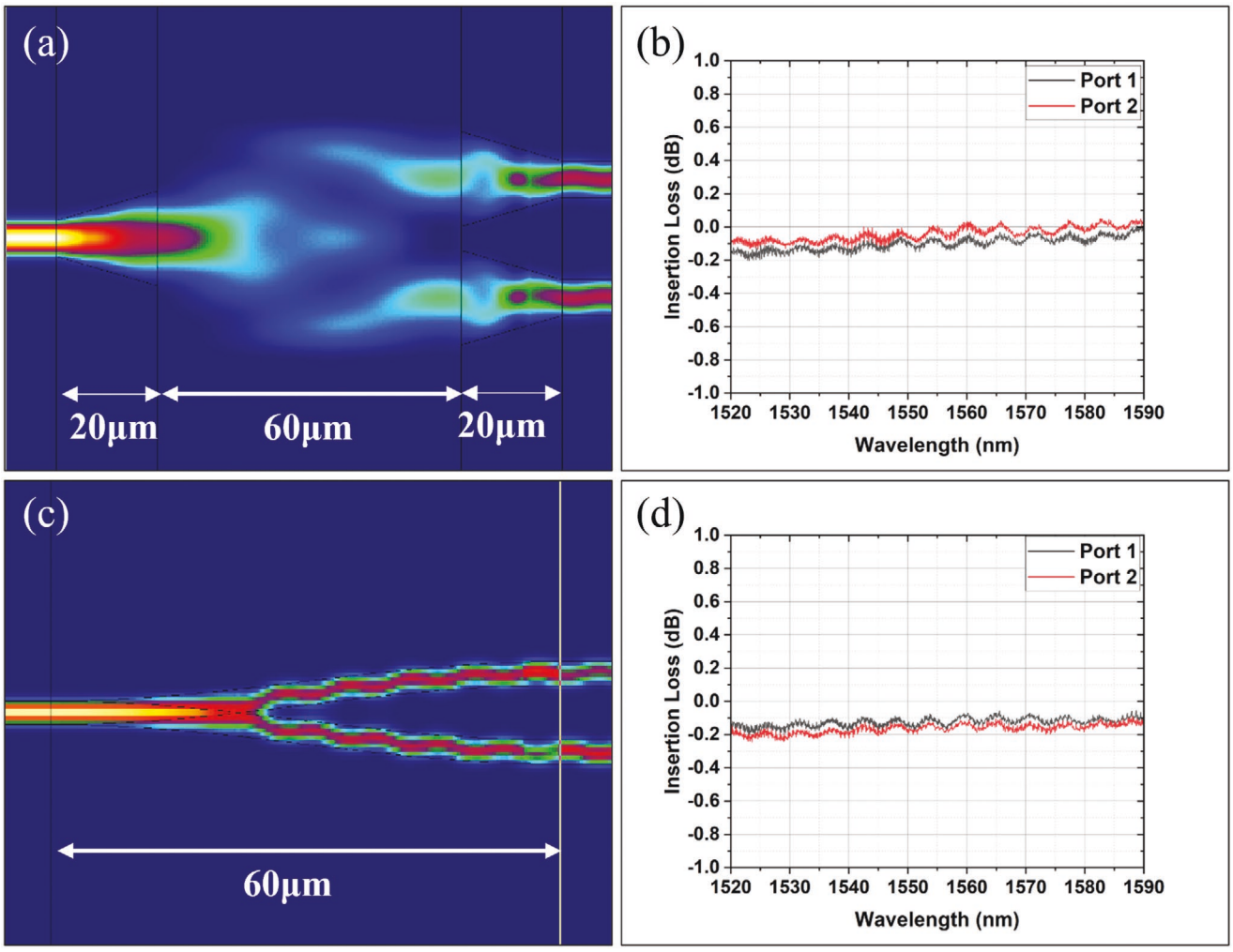

Figure 4. a) EME simulation for 1 × 2 MMI showing equal power splitting between the two ports; b) excess insertion loss measured in each arm of the 1 × 2 MMI; c) EME simulation for Y splitter with similar device length as the MMI with equal power splitting; and d) excess insertion loss measured in each arm of the Y splitter

many reports of polymer-based high Q resonators, the finesse of the polymer ring cavities is generally low. Our goal was to fabricate high Q resonators and high finesse cavities with a reduced area footprint enabled by the high RI of poly(S-*r*-DIB) while using standard coupling schemes at the key junctions in the device. Using the relationship between FSR and total device length,[41–44]

$$\mathrm{FSR} = \frac{\lambda_0^2}{n_g 2\pi R} \tag{1}$$

the radius of the rings (R) was chosen to be 200 μm to obtain a free spectral range (FSR) of 1.1 nm with a resonance wavelength, λ_0 of 1550 nm. We simulated the field distribution in the coupling region of the ring resonator using Lumerical software. The normalized electric field distribution (**Figure 5**a) shows the input light is partially coupled into the bend section of the ring and in the bus waveguide. Based on the resolution of e-beam resist, aspect ratio, and ease-of-fabrication, the gap between the straight section and the ring in the coupler region was chosen to be varied between 0.3 to 1.1 μm to allow for the determination of the critical coupling of the ring with the straight coupler section. The dimensions of the bus and the ring guiding elements were 2 μm wide and 0.45 μm high, similar to the other devices demonstrated above. As the bus waveguide-ring gap is increased, the resonator can be adjusted to span from under-coupled to critically coupled to over-coupled regimes. In most optimized devices, critically coupled ring resonators exhibit the largest extinction ratio. While larger gap values are desirable to accommodate for fabrication uncertainty, the precision enabled by our e-beam fabrication process (Figure 1c), specifically the near-vertical side-wall angle, allowed for the reduction of the bus waveguide-ring gaps to as small as 300 nm. The precise increments in the gap width of 100 nm helped us carefully study the coupling regimes and determine the critical coupling conditions. The output spectra of the rings with varying gaps are shown in Figure 5b. The transmission of devices with increasing gaps had similar insertion loss. As the gap increased from 0.3 to 1.1 μm, the extinction ratio increased since the coupling between the bus waveguide and ring

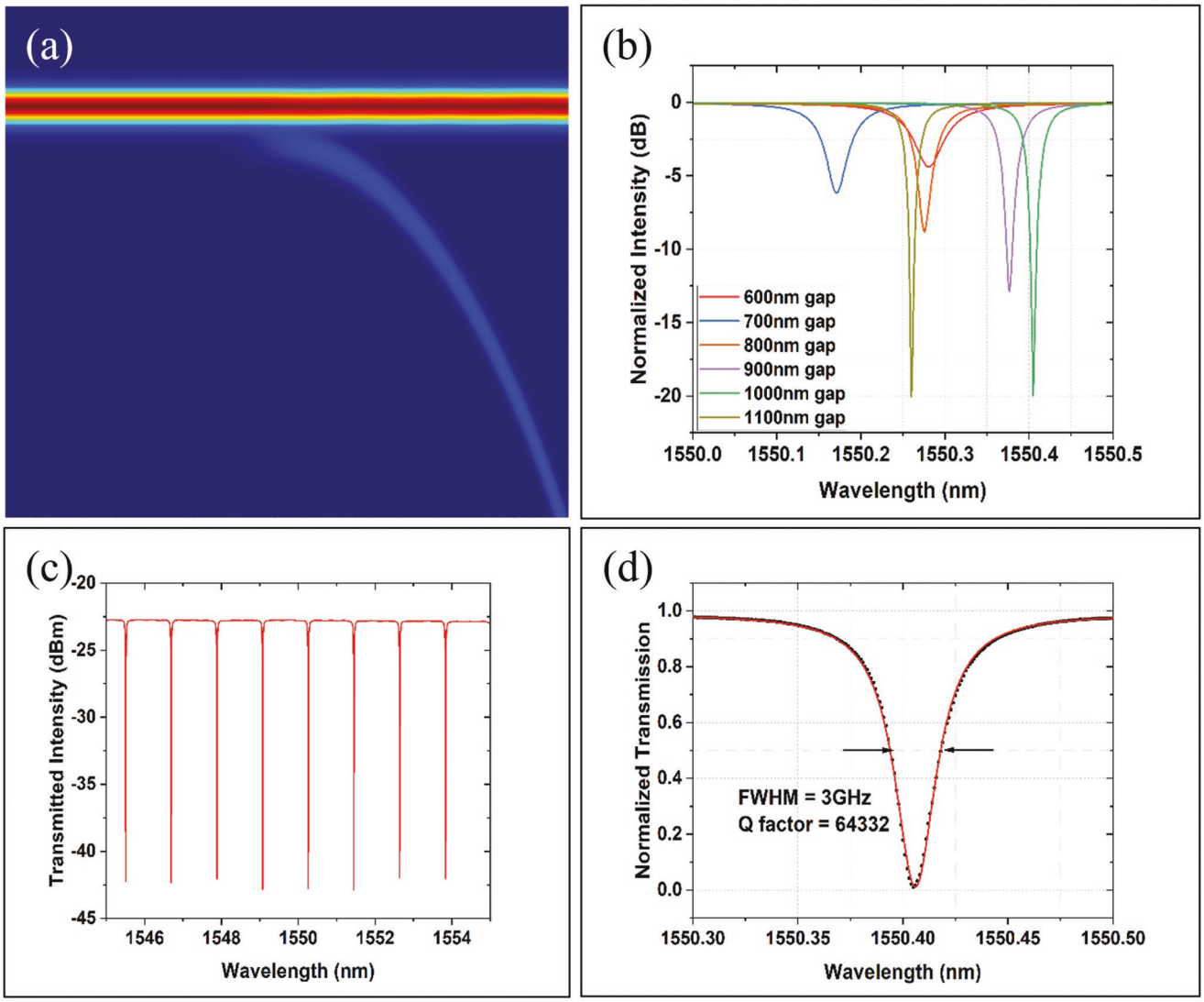

Figure 5. a) Normalized electric field distribution in the coupling region between bus waveguide and ring. b) Normalized intensity of ring resonators with a varying gap. The slight shift in resonance peak was due to fabrication imperfections and minimal change in the effective index. c) Output spectrum for a critically coupled ring with 20 dB extinction ratio and narrow linewidth. d) Normalized transmission for central peak at 1550.4059 nm with a full width half maximum of 3 GHz corresponding to a Q-factor of 64 332.

resonators transitioned from over-coupled to critically coupled. For narrow gaps under 600 nm,the ring resonator is in the over-coupling regime, and the resonance peaks are too shallow (low ER, < 5 dB) to be seen in the transmission spectrum, and hence were not shown in Figure 5b. As the gap increases from 300 to 600 nm, the resonance dips increasingly becomes deeper with about 5 dB ER (orange line, Figure 5b) observed for the 600 nm gap case. For rings with increasing gaps, the resonances become progressively stronger with narrower linewidths and a larger extinction ratio. The critically coupled operation was achieved for 1 µm gap indicated by the sharp decrease in resonance linewidth. The linewidths of the resonance peaks decreased from 1 to 0.02 nm for the critically coupled case. A very strong extinction ratio was observed for the ring resonator with a 1 µm gap (Figure 5c). The resonance (λ_0) was centered around 1550.4059 nm with an FSR of 1.1 nm which is very close to the designed value of 1550 and 1.09 nm respectively. The normalized resonance dips are fit to a Lorentzian, giving us a Q factor close to 65 000 with over 20 dB extinction ratio and a high finesse value of 45 for the cavity, as shown in Figure 5d. Strong coupling with large bus-ring gaps is highly encouraging and demonstrates the possibility of robust and high performance devices with large fabrication tolerance. Structures with even larger gaps can be made by incorporating racetrack structures or pulley couplers, as noted in the literature.[42] Further increase in the Q-factor is also expected as the coupling gap is increased and the ring is operated in the under-coupled regime with a larger bus-ring gap, resulting in a smaller extinction ratio and narrower linewidths.[41,45] To our knowledge, this is the first result demonstrating high performance ring resonators fabricated from high RI optical polymers that enabled both reductions of ring resonator radii while still retaining high

Table 1. Comparison of critical parameters for polymer micro-ring resonators.

Polymer resonator type	Refractive index	Ring radius [μm]	Q factor	Finesse	Reference
NOA71 microring	1.56	1000	57 500	8.84	[28]
Ormocore microring	1.55	220	39 400	14	[46]
PMMA microring	1.48	N.A.	1.1×10^5	N.A.	[47]
Polymer (N.A.) microring	1.46	5000	1.8×10^5	6.13	[49]
SU8 microring	1.56	200	3555	2.75	[50]
CHIPs microring	1.75	200	65 000	45	This work

Q-factors.[46–50] **Table 1** compares the refractive index of the core material, ring radius, measured Q-factor, and finesse values of our work with other polymer-based microring resonator work in the literature. The combination of these four parameters highlights the strong impact of our progress. In future work, we expect to fabricate ring resonators using the CHIPs-based platform with even smaller footprints with $Q > 10^6$ as often needed for gas sensing. The photonic devices demonstrated in this work highlight the potential of using processable CHIPs for photonic integration. With further improvements in material properties, polymers with RI above 2.0 can be used to demonstrate an all-polymer integrated photonic platform. The lower costs of the polymers combined with facile processing will help usher in the era of scaled-up, all-polymer photonic devices.

3. Conclusion

We have demonstrated for the first time a facile fabrication process for the production of single-mode photonic devices using high index CHIPs materials as a class of photonic polymers that exhibit excellent optical waveguide performance and record reductions in device feature size as integrated photonic elements in functioning devices. These findings highlight the benefits of the high RI and low optical losses of these materials, with waveguides fabricated using conventional lithography techniques. These advantages in conjunction with the low cost of these optical polymers due to the use of elemental sulfur point to the potential for scaling up the fabrication to wafer-level processes in realizing all-polymer photonic devices. In future work, we will pursue the incorporation of thermo-optic devices such as phase shifters, variable optical attenuators, tunable filters, and optical switches at telecommunication wavelengths and explore devices and longer IR wavelengths to extend the utility of this promising new polymer platform.

4. Experimental Section

Synthesis of poly(S-r-DIB) as the High RI core Material: The polymer was synthesized using the inverse vulcanization process.[14] In this process, the bulk sulfur powder was heated to 185 °C to form liquid sulfur, which was accompanied by a color change of the medium from yellow to red, indicating the conversion of the S_8 ring into liquid sulfur diradical followed by the formation of polymeric sulfur. At this point, a room-temperature aliquot of 1,3-diisopropenylbenzene (DIB) was added to the sulfur mixture, which resulted in a homogeneous yellow solution of much lower viscosity. After a short period of mixing and cooling at room temperature, the resulting formation was a transparent red polymeric glass which indicated the copolymerization of the DIB monomer with sulfur.

Fabrication Process of Photonic Devices: The polymer was spin-coated on a silicon wafer with a 6 μm thick thermally evaporated silicon dioxide layer, which served as the lower cladding for the waveguide. The oxide layer was thick enough to isolate the light from the higher index silicon substrate underneath. Poly(S_{70}-*r*-DIB_{30}) was made by the inverse vulcanization method as described above. The resulting glassy, the red polymer was then crushed into fine powder to dissolve into the solvent. The polymer was dissolved in chlorobenzene (350 mg mL^{-1} concentration) at 115 °C for 15 min until no visible particles were observed. The polymer was then left overnight to cool and to allow for any excess unreacted sulfur to precipitate to the bottom of the glass vial. The dissolved solution was then filtered using a 0.2 μm PTFE membrane syringe filter to remove any undissolved particles or any remaining impurities in the solution. Before spin coating, the substrate was cleaned with acetone and isopropanol (IPA), blown dry with nitrogen, and then O_2 plasma cleaned for 2 min to remove any organic impurities and improve the adhesion of the polymer to the surface. The polymer was then spin-coated at 3000 rpm with 500 rpm s^{-1} acceleration for 30 s. The remaining solvent was evaporated by heating the wafer at 110 °C for 5 min; the resulting film was 450 nm thick. The long bake time was necessary for removing any solvent and thermally crosslinking the polymer, which improved adhesion, etch resistance, and chemical compatibility. After the wafer cooled down to room temperature, the EBL resist maN2403 was spin coated directly on top of the polymer at 4000 rpm with 500 rpm s^{-1} acceleration for 30 s, followed by baking at 95 °C for 1 min resulting in 275 nm thick resist layer. The photonic circuit was then written using an Elionix EBL system with an optimized dose of 450 μC cm^{-2}. Once the e-beam exposure was completed, the exposed pattern was developed in the maD525 developer for 45–60 s. To transfer the pattern from the resist onto the polymer, the sample was etched using a fluorine-oxygen-argon etch in an inductively coupled plasma etcher (Plasmatherm ICP RIE). The etching recipe was specifically designed for the CHIPs family of polymers and comprised a mixture of CHF_3, O_2, and Ar gases. CHF_3 created fluoride radicals which removed the sulfur units from the sulfur copolymer, while O_2 etched the organic part of the polymer, and Ar made the etching anisotropic resulting in vertical sidewalls. RF and ICP power were also optimized to control the etch rate, sidewall roughness, and reduce redeposition (grass formation) on the substrate. The bottom silicon dioxide cladding layer had a much lower etch rate than the polymer for this etching recipe and acted as an etch stop to signal the etch's completion. The resulting etch rate of CHIPs was 312 nm min^{-1}, and the etch rate of maN2403 was 192nm min^{-1}; hence the resist could act as an effective etch mask. The thicknesses of the polymer and resist layers were optimized to ensure that the resist was fully etched away while the polymer was through etched. Any remaining resist could be removed by rinsing the sample with acetone/IPA. The etched waveguides had smooth sidewalls and nearly 90° sidewall angles. The high quality of the fabricated devices is shown in Figure 2. Once the etching was done, Chemoptics ZPU (n = 1.43) was spin-coated on the sample as a top cladding with 4 μm thickness and UV cured under N_2 atmosphere to crosslink the

ZPU layer. The fabrication process flow is shown in Figure 1c. The final fabricated device was prepared for optical characterization by cleaving the end facets with a diamond scribe. The waveguides could be accessed after cleaving and easily butt coupled to an optical fiber to launch the input light and collect the output light.

Optical Characterization Setup for Testing Photonic Devices: The devices were characterized by end-fire coupling single-mode SFM28 fibers to the waveguides at the input and output. The sample was placed on a sample stage while the fibers were mounted in a six-axis Thorlabs fiber stage. The waveguides were tested at 1310 and 1550 nm using a Thorlabs DFB laser centered at each of those wavelengths. The output light was first collimated by a 10X microscope objective lens which was then imaged by an InGaAs camera to observe the mode profile of the waveguide as shown in the Figure 3a inset. Once the mode was observed, the lens at the output was replaced by another SMF28 fiber connected to a Newport power meter to measure the total insertion loss of the device. To minimize the Fresnel loss at the input and output interfaces, Cargille index matching oil ($n = 1.47$) was used at both interfaces. After the fibers were aligned to the waveguide, the total insertion loss was measured. For the characterization of the splitters and ring resonators, the DFB laser was switched with an Agilent 8164A tunable laser source. The laser was swept from 1520 to 1580 nm with 50 pm sampling resolution. The output light was recorded by the Yokogawa AQ6370B optical spectrum analyzer (OSA) which was synced to the Agilent laser. For the ring resonators, the sampling resolution was increased to 1 pm to capture the narrow linewidth of the rings.

Acknowledgements

The authors acknowledge National Science Foundation (PFI-RP 1940942, MRI-1920234, DMREF-2118578, CHE-1807395, MRI-ECCS-1725571), the Air Force Research Laboratories (FA8650-16-D-5404), the RII Research Advancement Grant program, and the Hitachi Electron Microscopy scholarship for support of this work.

Conflict of Interest

The authors declare no conflict of interest.

Data Availability Statement

The data that support the findings of this study are available from the corresponding author upon reasonable request.

Keywords

high refractive index, integrated photonics, polymers, ring resonators, waveguides

Received: January 24, 2022
Revised: March 27, 2022
Published online: May 29, 2022

[1] H. Ma, A. K.-Y. Jen, L. R. Dalton, *Adv. Mater.* **2002**, *14*, 1339.
[2] L. Eldada, L. W. Shacklette, *IEEE J. Sel. Top. Quantum Electron.* **2000**, *6*, 54.
[3] H. Zuo, S. Yu, T. Gu, J. Hu, *Opt. Express* **2019**, *27*, 11152.
[4] K. Yasuhara, F. Yu, T. Ishigure, *Opt. Express* **2017**, *25*, 8524.
[5] J. W. Kang, J. P. Kim, W. Y. Lee, J. S. Kim, J. S. Lee, J. J. Kim, *J. Light. Technol.* **2001**, *19*, 872.
[6] M. Rezem, A. Gunther, B. Roth, E. Reithmeier, M. Rahlves, *J. Lightwave Technol.* **2017**, *35*, 299.
[7] R. Dangel, J. Hofrichter, F. Horst, D. Jubin, A. La Porta, N. Meier, I. M. Soganci, J. Weiss, B. J. Offrein, *Opt. Express* **2015**, *23*, 4736.
[8] N. Lindenmann, G. Balthasar, D. Hillerkuss, R. Schmogrow, M. Jordan, J. Leuthold, W. Freude, C. Koos, *Opt. Express* **2012**, *20*, 17667.
[9] P. O. Weigel, J. Zhao, K. Fang, H. Al-Rubaye, D. Trotter, D. Hood, J. Mudrick, C. Dallo, A. T. Pomrene, A. L. Starbuck, C. T. DeRose, A. L. Lentine, G. Rebeiz, S. Mookherjea, *Opt. Express* **2018**, *26*, 23728.
[10] M. Gehl, N. Boynton, C. Dallo, A. Pomrene, A. Starbuck, D. Hood, D. C. Trotter, A. Lentine, C. T. DeRose, *Opt. Express* **2018**, *26*, 18082.
[11] D. Duchesne, M. Ferrera, L. Razzari, R. Morandotti, B. Little, S. T. Chu, D. J. Moss, arXiv preprint:1505.05953 **2015**, 1.
[12] D. J. Moss, R. Morandotti, A. L. Gaeta, M. Lipson, *Nat. Photonics* **2013**, *7*, 597.
[13] H. W. M. Salemink, F. Horst, R. Germann, B. J. Offrein, G. L. Bona, *MRS Online Proc. Libr.* **1999**, *574*, 255.
[14] Y. Zou, L. Moreel, H. Lin, J. Zhou, L. Li, S. Danto, J. D. Musgraves, E. Koontz, K. Richardson, K. D. Dobson, R. Birkmire, J. Hu, *Adv. Opt. Mater.* **2014**, *2*, 759.
[15] Y. Zha, M. Waldmann, C. B. Arnold, *Opt. Mater. Express* **2013**, *3*, 1259.
[16] C. Tsay, F. Toor, C. F. Gmachl, C. B. Arnold, *Opt. Lett.* **2010**, *35*, 3324.
[17] X. Xia, Q. Chen, C. Tsay, C. B. Arnold, C. K. Madsen, *Opt. Lett.* **2010**, *35*, 3228.
[18] T. Higashihara, M. Ueda, *Macromolecules* **2015**, *48*, 1915.
[19] M. D. Alim, S. Mavila, D. B. Miller, S. Huang, M. Podgórski, L. M. Cox, A. C. Sullivan, R. R. McLeod, C. N. Bowman, *ACS Materials Lett.* **2019**, *1*, 582.
[20] M. D. Alim, D. J. Glugla, S. Mavila, C. Wang, P. D. Nystrom, A. C. Sullivan, R. R. McLeod, C. N. Bowman, *ACS Appl. Mater. Interfaces* **2018**, *10*, 1217.
[21] R. Hifumi, I. Tomita, *Polym. J.* **2018**, *50*, 467.
[22] H. Kim, B.-C. Ku, M. Goh, H. C. Ko, S. Ando, N.-H. You, *Macromolecules* **2019**, *52*, 827.
[23] Y. Su, E. B. D. S. Filho, N. Peek, B. Chen, A. E. Stiegman, *Macromolecules* **2019**, *52*, 9012.
[24] D. H. Kim, W. Jang, K. Choi, J. S. Choi, J. Pyun, J. Lim, K. Char, S. G. Im, *Sci. Adv.* **2020**, *6*, abb5320.
[25] Y. Tokushita, S. Furuya, S. Nobe, K. Nakabayashi, S. Samitsu, H. Mori, *Polymer* **2021**, *237*, 124346.
[26] Y. Huang, G. T. Paloczi, J. Scheuer, A. Yariv, *Opt. Express* **2003**, *11*, 2452.
[27] M. H. M. Salleh, A. Glidle, M. Sorel, J. Reboud, J. M. Cooper, *Chem. Commun.* **2013**, *49*, 3095.
[28] A. V. Shneidman, K. P. Becker, M. A. Lukas, N. Torgerson, C. Wang, O. Reshef, M. J. Burek, K. Paul, J. McLellan, M. Lončar, *ACS Photonics* **2018**, *5*, 1839.
[29] W. J. Chung, J. J. Griebel, E. T. Kim, H. Yoon, A. G. Simmonds, H. J. Ji, P. T. Dirlam, R. S. Glass, J. J. Wie, N. A. Nguyen, B. W. Guralnick, J. Park, Á. Somogyi, P. Theato, M. E. Mackay, Y. E. Sung, K. Char, J. Pyun, *Nat. Chem.* **2013**, *5*, 518.
[30] L. E. Anderson, T. S. Kleine, Y. Zhang, D. D. Phan, S. Namnabat, E. A. LaVilla, K. M. Konopka, L. Ruiz Diaz, M. S. Manchester, J. Schwiegerling, R. S. Glass, M. E. Mackay, K. Char, R. A. Norwood, J. Pyun, *ACS Macro Lett.* **2017**, *6*, 500.
[31] J. J. Griebel, S. Namnabat, E. T. Kim, R. Himmelhuber, D. H. Moronta, W. J. Chung, A. G. Simmonds, K. J. Kim, J. Van Der Laan, N. A. Nguyen, E. L. Dereniak, M. E. MacKay, K. Char, R. S. Glass, R. A. Norwood, J. Pyun, *Adv. Mater.* **2014**, *26*, 3014.
[32] B. J. Eggleton, B. Luther-Davies, K. Richardson, *Nat. Photonics* **2011**, *5*, 141.
[33] T. S. Kleine, R. S. Glass, D. L. Lichtenberger, M. E. Mackay, K. Char, R. A. Norwood, J. Pyun, *ACS Macro Lett.* **2020**, *9*, 245.

[34] T. S. Kleine, L. R. Diaz, K. M. Konopka, L. E. Anderson, N. G. Pavlopolous, N. P. Lyons, E. T. Kim, Y. Kim, R. S. Glass, K. Char, R. A. Norwood, J. Pyun, *ACS Macro Lett.* **2018**, *7*, 875.
[35] N. P. Lyons, A. Nishant, L. E. Anderson, T. S. Kleine, K. M. Konopka, J. Pyun, R. A. Norwood, in *Optical Components and Materials XVI* (Eds: S. Jiang, M. J. F. Digonnet), SPIE, San Francisco, CA **2019**.
[36] M. D. Islam, J. O. Kim, Y. Ko, Z. Ku, D. A. Boyd, E. M. Smith, V. Q. Nguyen, J. D. Myers, C. C. Baker, W. Kim, J. S. Sanghera, D. A. Czaplewski, A. M. Urbas, J. Genzer, J. E. Ryu, *Macromol. Mater. Eng.* **2020**, 305.
[37] C. Tavella, P. Lova, M. Marsotto, G. Luciano, M. Patrini, P. Stagnaro, D. Comoretto, *Crystals* **2020**, *10*, 154.
[38] Y. O. Noh, H. J. Lee, Y. H. Won, M. C. Oh, *Opt. Commun.* **2006**, *258*, 18.
[39] S.-M. Kim, E.-S. Lee, K.-W. Chun, J. Jin, M.-C. Oh, *Sci. Rep.* **2021**, *11*, 10576.
[40] C.-Y. Chao, L. J. Guo, *J. Lightwave Technol.* **2004**, *24*, 1395.
[41] W. Bogaerts, P. de Heyn, T. van Vaerenbergh, K. de Vos, S. Kumar Selvaraja, T. Claes, P. Dumon, P. Bienstman, D. van Thourhout, R. Baets, *Laser Photonics Rev.* **2012**, *6*, 47.
[42] D. G. Rabus, C. Sada, *Integrated Ring Resonators: A Compendium*, 2nd ed., Springer, Cham, Switzerland **2020**.
[43] D. P. Cai, J. H. Lu, C. C. Chen, C. C. Lee, C. E. Lin, T. J. Yen, *Sci. Rep.* **2015**, *5*, 10078.
[44] P. Ma, D.-Y. Choi, Y. Yu, Z. Yang, K. Vu, T. Nguyen, A. Mitchell, B. Luther-Davies, S. Madden, *Opt. Express* **2015**, *23*, 19969.
[45] E. E. Hach, A. W. Elshaari, S. F. Preble, *Phys. Rev. A: At., Mol., Opt. Phys.* **2010**, *82*, 063839.
[46] R. Morarescu, P. K. Pal, N. T. Beneitez, J. Missinne, G. V. Steenberge, P. Bienstman, G. Morthier, *IEEE Photonics J.* **2016**, *8*, 1.
[47] T. Ling, S.-L. Chen, L. J. Guo, *Opt. Express* **2011**, *19*, 861.
[48] X. Tu, S.-L. Chen, C. Song, T. Huang, L. J. Guo, *IEEE Photonics J.* **2019**, *11*, 1.
[49] G. Qian, J. Tang, X.-Y. Zhang, R.-Z. Li, Y. Lu, T. Zhang, *J. Nanomater.* **2014**, *2014*, 146510.
[50] J. K. S. Poon, Y. Huang, G. T. Paloczi, A. Yariv, *IEEE Photonics Technol. Lett.* **2004**, *16*, 2496.